Supply- and Load-Modulated Balanced Amplifier for Efficient Broadband 5G Base Stations

Tommaso Cappello, *Member, IEEE*, Prathamesh Pednekar, *Student Member, IEEE*, Corrado Florian, *Member, IEEE*, Steve Cripps, *Life Fellow, IEEE*, Zoya Popovic, *Fellow, IEEE*, and Taylor W. Barton, *Senior Member, IEEE*

***Abstract*— This paper presents a broadband efficient power amplifier (PA) targeting sub-6-GHz 5G base station applications. Due to the demanding requirements in both peak-to-average power ratio (PAPR) and bandwidth in 5G systems, we employ a combination of both load and supply modulation for efficiency enhancement. Active matching, implemented using an RF-input load-modulated balanced amplifier (LMBA) architecture, enables efficient octave-bandwidth operation. Supply modulation, which is carrier frequency agnostic, is then used to further extend the back-off efficiency. This paper focuses on a study of supply modulation strategies for the load-modulated PA using an efficient GaN eight-level discrete supply modulator. To overcome the bandwidth limitations associated with discrete-level switching, a commutation rate reduction (CRR) filter is applied in digital baseband and its effects are analyzed theoretically and experimentally. The supply-modulated LMBA is characterized across 1.8–3.8 GHz with 100-MHz, 10-dB PAPR signals. An output power of 34 dBm with average composite (total) PAE ranging from 22.4% to 43.9% across the band is demonstrated, with an ACLR of about −50 dBc after digital predistortion.**

***Index Terms*— Base station, carrier aggregation (CA), digital predistortion (DPD), fifth generation (5G) network, new radio (NR), orthogonal frequency-division multiplexing (OFDM), peak-to-average power ratio (PAPR), power amplifier (PA), power-DAC, supply modulation (SM), waveform.**

I. Introduction

INCREASING demands for high data rates, reduced latency, and increased device density are driving the development of fifth generation (5G) wireless systems. To support these needs, both millimeter-wavebands and existing radio resources below 6 GHz will be employed. As with 4G, downlink transmission in 5G systems will be based on orthogonal frequency-division multiplexing (OFDM), with system advantages including high spectral efficiency, low computational complexity, and ease of integration in multiple-in multiple-out (MIMO) systems [1].

Manuscript received November 12, 2018; revised February 1, 2019; accepted February 7, 2019. Date of publication May 27, 2019; date of current version July 1, 2019. *(Corresponding author: Taylor W. Barton.)*

T. Cappello, P. Pednekar, Z. Popovic, and T. W. Barton are with the Department of Electrical, Computer and Energy Engineering, University of Colorado Boulder, Boulder, CO 80304 USA (e-mail: tommaso.cappelo@colorado.edu; taylor.w.barton@colorado.edu).

C. Florian is with the Department of Electrical, Electronic, and Information Engineering, University of Bologna, 40136 Bologna, Italy.

S. Cripps is with the School of Engineering, Cardiff University, Cardiff CF10 3AT, U.K.

Color versions of one or more of the figures in this paper are available online at http://ieeexplore.ieee.org.

Digital Object Identifier 10.1109/TMTT.2019.2915082

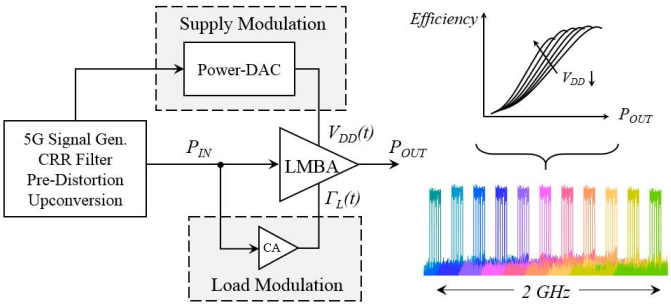

Fig. 1. Conceptual block diagram of the proposed architecture for 5G base stations. An SM-LMBA is used to efficiently transmit high-PAPR waveforms across a 1.8–3.8-GHz band. Supply modulation provides frequency-independent back-off efficiency enhancement, while load modulation allows for broadband impedance match.

OFDM signals, however, are challenging for efficient power amplifier (PA) design due to high peak-to-average power ratio (PAPR) and high instantaneous bandwidth. An additional demand on the PA is operation over a broad RF bandwidth in order to reduce the number of PAs in an agile radio environment, which exacerbates the challenge of high-efficiency operation. In this paper, we present a PA architecture with simultaneous broad RF bandwidth, high back-off efficiency over the band, and the ability to amplify multiple concurrent signals with large instantaneous bandwidth. The approach, illustrated in Fig. 1, combines load and supply modulation (SM) to improve efficiency over a wide range of output power levels, while frequency agility and linearization are enabled by a flexible digital baseband design.

The challenge of high signal PAPRs can be addressed through signal design, PA design, or a combination of both. Digital signal processing (DSP) techniques, for example, clipping, crest factor reduction, or partial transmit sequence techniques [2], can be used to reduce the signal PAPR. Drawbacks generally include increased digital complexity, decreased spectral efficiency, and reduced flexibility in waveform design.

From a circuit design perspective, on the other hand, the PA can be designed to maintain high performance over a wide range of output power levels through efficiency enhancement techniques. Load modulation achieves efficiency enhancement in back off with a minimum of two PAs that interact through

active loading, such as in the case of Doherty [3]–[6] and Chireix outphasing [7]–[10] PAs. In these active matching techniques, additional power is consumed by the modulating device and is reused by the circuit architecture. For example, a passive inverting element in the Doherty configuration helps recover the auxiliary power at the output; however, this is a bandwidth limitation and can only be used for modulating the main device impedance along the real axis. The load-modulated balanced amplifier (LMBA), introduced in [11]–[14], is an important new development where the main device impedance can be modulated both resistively and reactively, while whatever power required from the auxiliary control device is fully recovered at the output. This enables the LMBA to be used in broadband applications, as shown in [14].

An alternative efficiency enhancement method is SM, in which a dynamic power supply tracks the signal envelope according to some "trajectory" [15]. In SM transmitters, the dynamic supply modulator's efficiency degrades with an increased signal bandwidth, limiting the total (composite) transmitter efficiency. Typical supply modulators consist of an efficient slow switcher and a linear fast amplifier [16], [17] and are limited to relatively narrowband signals considering the 5–10 times bandwidth expansion of the envelope relative to the IQ bandwidth. The required supply modulator slew rate can be reduced with shaping functions [18], [19] or through power envelope tracking, see [20]. Another approach is to switch the supply between several discrete levels for coarse amplitude control, sacrificing linearity. This approach is applied successfully to single-ended PAs with drain [21], as well as gate and drain modulation [22], for large bandwidth signals. Load-modulated PAs can be further enhanced with SM, demonstrated with Doherty [23]–[25] and Chireix outphasing PAs [26].

In this paper, we leverage the combined benefits of supply and load modulation to develop a PA with efficiency enhancement over a wide range of both output power and frequency, with the sub-6-GHz octave-bandwidth 5G downlink applications as a target. Active load modulation performs the octave-bandwidth active match, and SM enhances back-off efficiency. Reconfigurability and frequency agility are enabled by a flexible digital baseband design employing digital predistortion (DPD). A primary contribution of this paper is in demonstrating SM applied to a more complicated and broadband "base" PA, required for 5G systems, as compared to previous supply-modulated transmitter demonstrations. Additionally, we demonstrate that DPD can be employed for 100-MHz high-PAPR signals to maintain the ACLR below -50 dBc over the entire 1.8–4-GHz band, with a time-average composite power-added efficiency ranging from 22.4% at the high end to 43.9%, including both the PA and the supply modulator efficiency.

This paper expands on the related conference paper [27], which demonstrated initial envelope-tracking results with the RF-input LMBA (ET-LMBA) for a 20-MHz LTE signal. Here, we present an analysis of the RF-input LMBA under more general SM (SM-LMBA) and perform a detailed investigation with 100-MHz signals over an octave bandwidth. Section II provides detail on the LMBA design and characterization for SM. Signal requirements for 5G relevant to PA design are discussed in Section III, along with digital baseband challenges associated with wideband discrete-level SM. Section IV presents the experimental system operating over 1.8–4 GHz with 100-MHz, 10-dB PAPR signals, with a study of how linearity and efficiency tradeoff over bandwidth and PAPR.

II. Supply-Modulated LMBA

Implementation of SM architectures can be characterized as belonging to one of two modes. The term envelope tracking (ET) usually refers to a mode in which the RF device is operated linearly, i.e., the amplitude of the output voltage swing remains lower than the supply voltage at all times. In this approach, the gain and matching conditions are not substantially modulated by the supply voltage variation, and the output power remains a nominally linear function of the input signal drive level.

More generally, dynamic SM can allow clipping on the supply rails at some predetermined supply level. In practice, the transition between these two SM modes will not be clearly defined, due in main part to the gradual incursion of the I–V trajectory into the knee region of the device characteristics. Such incursion is almost inevitable when high-efficiency operation is being sought, and this applies especially when using GaN devices which usually display a relatively soft knee characteristic. In both cases, some significant modulation of the device gain and matching characteristics will result from the large supply variations, and if conventional, fixed passive matching is used and this may result in nonlinear effects which cannot be fully corrected using DPD. This problem is compounded when attempting to design a broadband RFPA, where passive matching networks cannot, in practice, be designed to present optimum load impedances over the extended RF bandwidth. In this paper, the novel use of simultaneous, real-time load modulation is employed to compensate for the changes in gain and impedance caused by the SM and to do so over an octave RF bandwidth.

A. SM-LMBA Architecture

A simplified block diagram of the SM-LMBA is shown in Fig. 2. At the core of this architecture is the RF-input LMBA [14], in which the two amplifiers comprising a balanced amplifier (BA) are load modulated by a control PA. Details of the design and implementation of the RF-input LMBA used in this paper are given in [14] and summarized below. Initial experiments with SM are described in [27], in which the system is demonstrated with a 20-MHz, 10-dB PAPR signal.

In the RF-input LMBA architecture, the control PA drive signal is derived from the RF input through a coupler. Dynamic load modulation is achieved by implementing the control PA with a small-periphery device (here, the CGH40006 6-W device from Wolfspeed) relative to those in the BA (each 10 W, i.e., Wolfspeed CGH40010) so that it compresses at a lower input power than the BA. Therefore, the *relative* level of the injected control signal compared to that of the BA varies

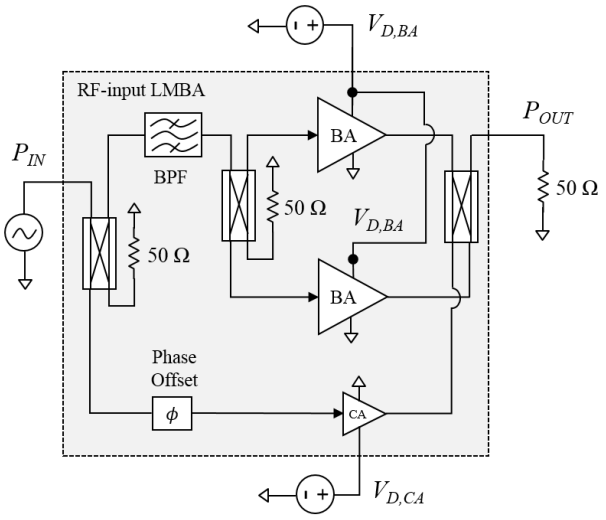

Fig. 2. Block diagram of the RF-input LMBA [14]. A control signal derived from the RF input modulates the impedance "seen" by the BA devices.

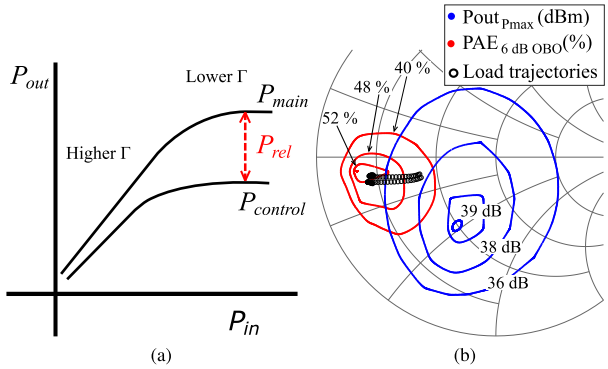

Fig. 3. RF-input LMBA operation under nominal supply conditions $V_{D,BA} = 28$ V and $V_{D,CA} = 20$ V. (a) Asymmetric sizing of the control and balanced PA paths generates an input power-dependent difference between the main and control amplifier levels. (b) As input power increases, the load moves toward the center of the Smith chart [14].

over power, as illustrated in Fig. 3. The BA is matched for efficiency at 6-dB output back off (OBO). As the relative power P_{rel} of the main signal increases (i.e., at high output powers), the reflection coefficient "seen" by the BA devices moves toward the center of the Smith chart, where the BA output power is higher.

To achieve this load modulation characteristic across an octave bandwidth, a bandpass filter (BPF) is inserted in the BA path (see Fig. 2). This octave-bandwidth BPF does not affect the amplitude response of the LMBA but produces a frequency-dependent phase between the BA and control paths. By appropriately designing the filter response [Fig. 4(a)], the target load impedance of the BA devices (found from simulated load–pull) is tracked across frequency [Fig. 4(b)].

Fig. 4(b) shows the simulated nominal design case as developed in [14], i.e., $V_{D,BA} = 28$ V and $V_{D,CA} = 20$ V. The load trajectories behave as desired: they nearly intersect the load corresponding to maximum PAE at each of the shown frequencies, tracking the counterclockwise rotation in the Smith chart. In measurement, we find that performance is slightly enhanced by operating the BA instead at $V_{D,BA} = 30$ V due to

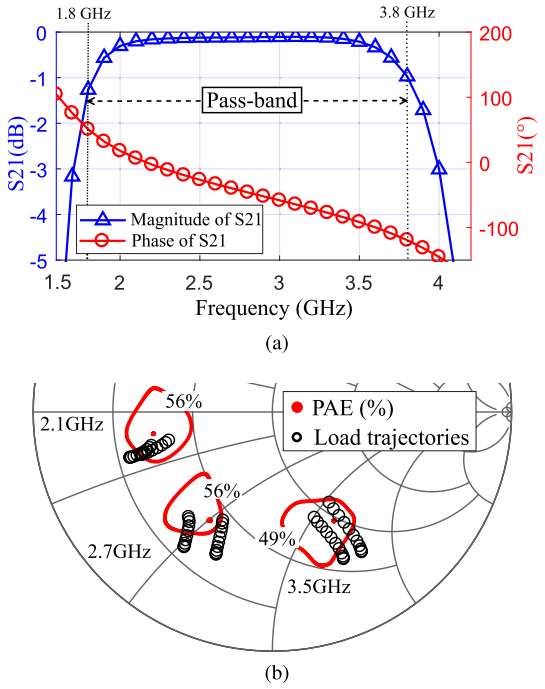

Fig. 4. Active match across the octave bandwidth is achieved by inserting a BPF in the BA path. (a) BPF frequency response [14]. (b) Simulated load impedance trajectories across frequency for the nominal supply condition as simulated in [14], i.e., $V_{D,BA} = 28$ V and $V_{D,CA} = 20$ V [27].

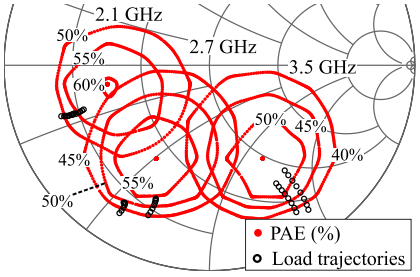

Fig. 5. Simulated load impedance trajectories across frequency when $V_{D,BA} = 20$ V and $V_{D,CA} = 20$ V, corresponding to approach (2) or (3).

slight differences between simulated and measured behaviors. When SM is then applied to one or both of the BA and control amps, the back-off efficiency of the individual amplifier is expected to further improve. As seen in [27], however, at the LMBA architectural level, SM modifies the asymmetric behavior of the BA and control amps because the relative power of the two amplifiers depends on their respective supply voltages. For example, Fig. 5 shows the load modulation trajectories of the BA devices when $V_{D,BA} = V_{D,CA} = 20$ V. Compared to the nominal conditions in Fig. 4, the BA trajectories do not intersect the peak PAE contours found from the load–pull simulation of the device. Therefore, it is not immediately clear whether SM will improve the RF-input LMBA performance. To investigate this further, the LMBA performance is characterized by five possible SM cases.

1) No SM.
2) SM of both the balanced and control amplifiers together, i.e., with $V_{D,BA} = V_{D,CA}$.

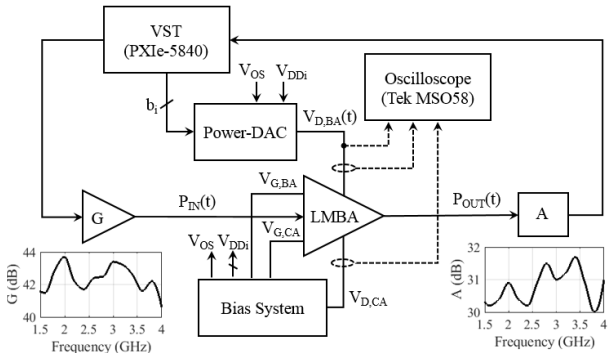

(a)

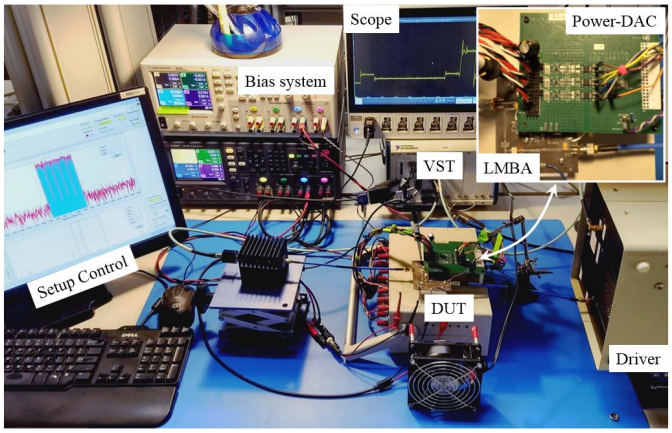

(b)

Fig. 6. (a) Block diagram of the experimental setup. A broadband calibration from 1.5 to 4 GHz is performed to calibrate the setup at the LMBA input and output connectors. The drain voltage and currents are monitored with a sampling oscilloscope for characterization purposes. The modulated signals are generated by a 1-GHz NI VST. (b) Photograph of the experimental setup with an enlarged picture of the ET-LMBA in the inset.

3) SM of the BA only, with the control amplifier supply voltage held fixed at its nominal value of $V_{D,CA} = 20$ V.
4) SM of the BA only, with the control amplifier supply voltage fixed but increased to $V_{D,CA} = 30$ V, thereby reducing the extent of compression in the CA.
5) SM of both the balanced and control amplifiers, with a fixed ratio of the two voltages such that $V_{D,CA} = 0.8 \times V_{D,BA}$, corresponding to the ratio of these voltages in the nominal design.

Of these, all but case 5 can be implemented using the experimental system. A potential sixth option is to supply modulate the control amplifier only, keeping the BA fixed at its nominal design voltage. However, intuition and simulations predict that this will not enhance back-off efficiency and so this case is not measured.

The block diagram and photograph of the experimental setup for this and subsequent measurements are shown in Fig. 6. A computer-controlled National Instruments Vector Signal Transceiver (VST) generates the modulated signal which is amplified by a benchtop driver (G) at the input $P_{\mathrm{IN}}(t)$ of the LMBA. The output power $P_{\mathrm{OUT}}(t)$ is attenuated (A) and sampled by the VST. An oscilloscope monitors the drain voltage of the BA, as well as the drain currents during the

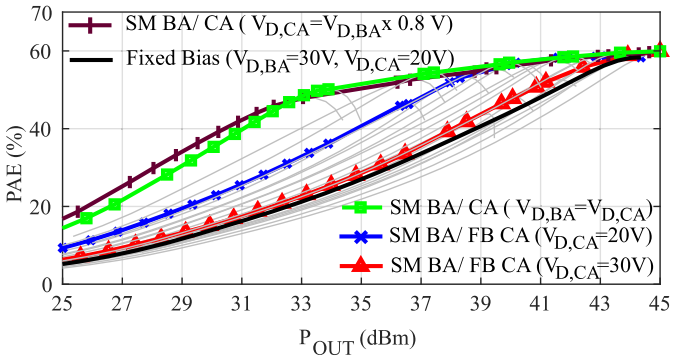

Fig. 7. Simulated SM-LMBA performance at 3 GHz for the five supply load modulation cases. (1) No SM, i.e., fixed bias (black). (2) SM of both PAs together, i.e., $V_{D,CA} = V_{D,BA}$ (green). (3) and (4) SM of BA only, with $V_{D,CA} = 20$ V (blue) and with $V_{D,CA} = 30$ V (red). (5) S SM of both as $V_{D,CA} = V_{D,BA} \times 0.8$ V (brown). Simulations include efficiency of the LMBA only.

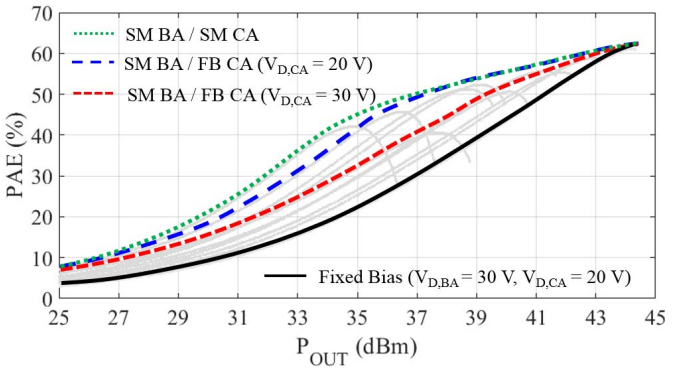

Fig. 8. Measured PAE trajectories at 2.1 GHz for various combinations of supply voltages (gray curves), and comparing four possible supply strategies of the SM-LMBA: without SM (black continuous curve), equal SM of both the control and balanced PAs (green dotted curve), and SM of the BA and fixed supply of the control PA (blue and red dashed curve). These measurements include the efficiency of the LMBA only.

characterization phase. Power calibration over frequency is performed at the input and output of the LMBA. Details of the supply modulator are given in Section IV.

Simulated results for various supply voltage combinations are shown in Fig. 7, while measurements with static supply voltages corresponding to cases (1)–(4) are shown in Fig. 8. These simulations and measurements are made with static supplies only, i.e., the supply modulator efficiency is not considered and no shaping function is applied. It can be seen that a fixed supply produces the lowest overall PAE, while supply modulating both PAs together gives the highest performance. Interestingly, measurement modulating both supplies together leads to only marginal PAE improvement, and only below 7-dB OBO. Although there is as much as a 5% point improvement in PAE at 10-dB OBO, the nearly identical performance in the higher power range leads us to conclude it is preferable to modulate the BA supply only. This is based on bandwidth considerations—the physical connection between the two supplies adds inductance that degrades the possible modulation bandwidth and can lead to timing mismatch between the two supply levels [21]. In the remainder

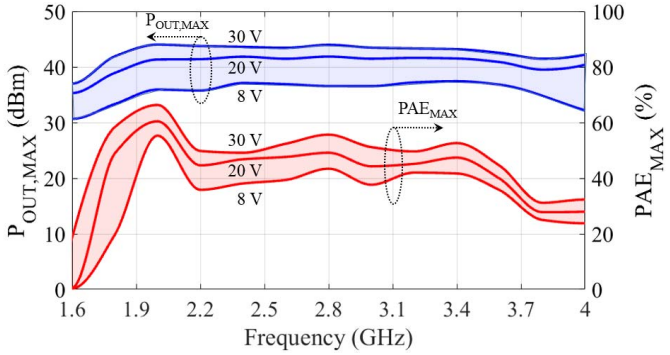

Fig. 9. $P_{\mathrm{OUT,MAX}}$ and $\mathrm{PAE_{MAX}}$ versus frequency for the minimum, intermediate, and maximum supply levels (8, 20, 30 V). Active load modulation performed by the control PA enables good impedance matching for high efficiency throughout the amplifier bandwidth.

of this paper, therefore, we supply modulate the BA and keep the control PA supply fixed.

Output power and PAE measurements across frequency for various BA supply voltages are shown in Fig. 9 when the BA alone is supply modulated. Peak output power is relatively flat across a 1.8–3.8-GHz range, whereas there is an efficiency peak at 2 GHz. The frequency-dependent amplifier gain and PAE also depend on supply level, as captured in Fig. 10 at 2.1 GHz. A supply shaping function [see Fig. 10 (right axis)] is used to select the BA supply voltage for a given desired output power level. Supply level selection tradeoffs gain flatness and PAE. In practice, the supply shaping function is discretized for use with the discrete-level supply modulator (Fig. 11), with a different shaping function required at each operating frequency.

III. Digital Baseband Signals and Generation

A. 5G Waveform Analysis

In order to understand the PA and digital baseband operating requirements in terms of bandwidth and dynamic range, we first examine the up- and down-link OFDM waveforms for 5G systems. In general, an OFDM signal can be expressed as [29]

$$x(t) = \sum_{k=1}^{N_C} x_k e^{j2\pi k\Delta f t} = \sum_{k=1}^{N_C} A_k e^{j(2\pi k\Delta f t + \phi_k)} \tag{1}$$

where $x_k = A_k e^{j\phi_k}$ is an array of complex symbols that modulate a set of N_C orthogonal subcarriers, and $\Delta f = 1/(N_C T)$ is the carrier frequency spacing, fixed in 4G systems to 15 kHz. For the higher bandwidth 5G signals, the carrier spacing is varied as

$$\Delta f = 2^{\mu} \times 15 \text{ kHz}. \tag{2}$$

Here, 15 kHz is the baseline 4G spacing and μ is the *numerology* [30] that can take on values of $0, 1, 2$ [31], leading to a subcarrier spacing of 15, 30, and 60 kHz in the sub-6-GHz bands. The maximum bandwidth for 5G is, therefore, between 50 MHz ($\Delta f = 15$ kHz) and 200 MHz ($\Delta f = 60$ kHz), which further increases the PAPR.

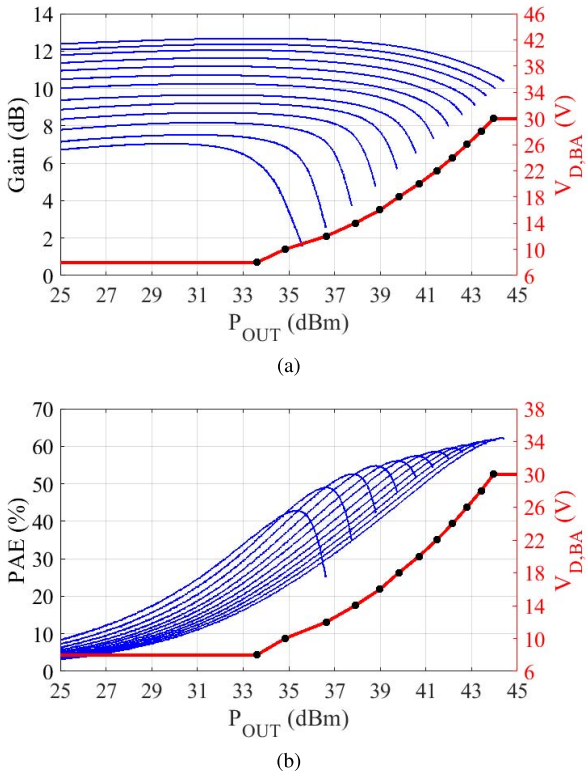

Fig. 10. Measured gain (a) and PAE (b) at 2.1 GHz for the SM-LMBA with variable drain supply between 8 and 30 V at 2-V steps for the BA and fixed supply voltage on the control PA (20 V). The gate biases are −2.6 V for the balanced and −3 V for the control PA. Superposed is the extracted trajectory of the supply shaping table.

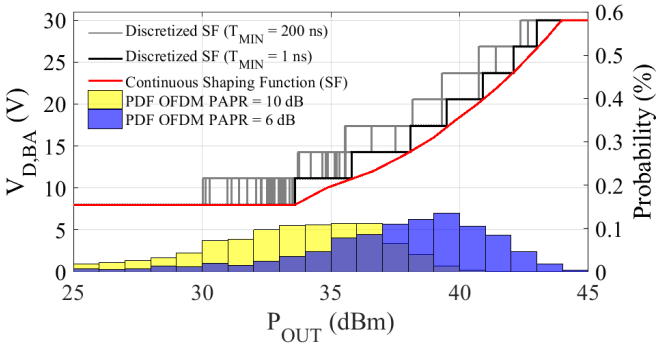

Fig. 11. Discretized shaping function as obtained by the continuous bias characterization. Eight equally spaced voltage levels are selected between 8 and 30 V. The threshold is selected accordingly to maximize intralevel efficiency. Two pdfs are superposed for OFDM signals with 512 carriers and two PAPRs (10 and 6 dB).

The probability that the PAPR of an OFDM signal exceeds a certain threshold value PAPR_0 can be expressed as

$$\mathrm{P}(\mathrm{PAPR} > \mathrm{PAPR}_0) \approx 1 - (1 - e^{-\mathrm{PAPR}_0})^{N_C} \tag{3}$$

assuming N_C is sufficiently large (> 64). The resulting probability is a complementary cumulative distribution function (CCDF), as shown in Fig. 12, which compares the PAPR CCDFs of an LTE/LTE-A OFDM signal within two extreme values of 72 and 1200 subcarriers [31] to that of 5G new radio (NR) as in Release 15 with two extreme values

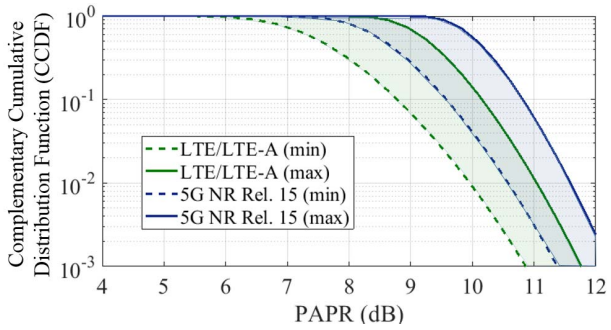

Fig. 12. Cumulative probability of PAPRs comparing OFDM signals for LTE/LTE-A ($72 < N_C < 1200$) and 5G NR ($333 < N_C < 6600$). Higher PAPRs are significantly more likely with the new generation of radio systems.

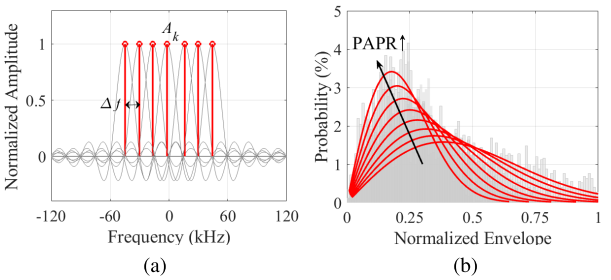

Fig. 13. Waveforms generated with the multisignal algorithm [28]. (a) Tone amplitude A_k and spacing Δf can be individually set, while the phase is used to achieve a predetermined PAPR. (b) Sequences with PAPRs ranging from 12 to 5 dB. For a high enough number of random, Gaussian distributed I/Qs, the envelope can be approximated with a Rayleigh probability density function (red contours).

of 333 and 6600 [31], [32]. The probability of higher PAPRs is significantly higher with the new generation radio systems, creating challenges for efficient PA design.

Various techniques have been proposed for PAPR reduction. The most common is clipping and filtering [33], [34] in which the signal is first clipped to a certain level and then filtered to reduce in- and out-of-band distortion. Other techniques such as selected mapping and partial transmit sequence carry high computational complexity and typically degrade bit error rate (BER). No one technique has been proven to be optimal for a given OFDM signal [34].

In this paper, which focuses on the SM-LMBA performance across frequency and PAPR, our goal is to characterize the PA with arbitrary signals corresponding to the range of PAPR values expected in 5G systems, as indicated in Fig. 12. Rather than generating an OFDM signal and applying reduction techniques, therefore, we use a multisignal algorithm detailed in [28] to generate an OFDM signal with an arbitrary number of subcarriers, band distribution, and PAPR (see Fig. 13). In this algorithm, the phase ϕ_k of the complex symbols x_k is controlled by an iterative algorithm to generate offline sequences of I/Qs with arbitrary PAPRs, band distributions, and Rayleigh pdf, which are useful to mimic the statistics of an OFDM signal for 5G from a PA standpoint.

B. Commutation Rate Reduction Filter

The wide bandwidths targeted for 5G communications, combined with the bandwidth expansion associated with

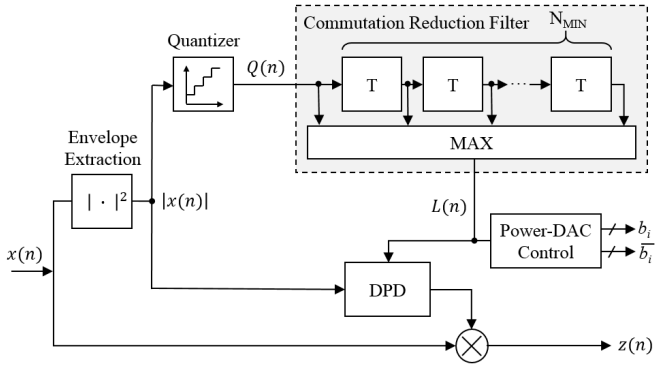

Fig. 14. Block diagram of the digital baseband. An envelope extraction block generates the envelope from the input I/Qs. A quantizer extracts the 3-bit representation of the original envelope and it is followed by the commutation reduction algorithm which generates the level of the supply modulator.

the envelope operation [35], makes conventional tracking challenging [36]. Therefore, it is necessary to limit the envelope bandwidth used to control the discrete supply modulator. In this paper, we employ a nonlinear filter to limit the commutation rate of the supply modulator and so decouple the signal bandwidth requirements from those of the supply modulator. The operation of the filter can be described as [35], [37]

$$L(n) = \max[Q(n), Q(n-1), \ldots, Q(n-N_{\text{MIN}})] \qquad (4)$$

where N_{MIN} is the number of taps of a delay line. The algorithm operates as a sliding window on $N_{\text{MIN}}+1$ samples, computing the maximum value within the window for every clock cycle, and generating an output $L(n) = Q(n)$ with a minimum pulse duration $T_{\text{MIN}} = 1/f_S$ for $N_{\text{MIN}} = 0$. For $N_{\text{MIN}} > 0$, the algorithm generates a sample $L(n)$ with an amplitude which is the maximum between $Q(n)$ and the N_{MIN} past samples, and with a minimum time duration T_{MIN} equal to $T \cdot (N_{\text{MIN}} + 1)$. Thus, the parameter N_{MIN} sets the minimum pulse duration at the output of the supply modulator, selected based on the capabilities of the hardware, e.g., the interface between the supply modulator and PA.

When the filter is placed after the quantizer, the digital hardware complexity of the algorithm is very low: a low bitwidth shift-register and a max computational block that can be efficiently implemented using comparators. The block diagram of the digital baseband with the commutation rate reduction (CRR) filter is shown in Fig. 14.

Fig. 15 demonstrates operation in the time domain with a 100-MHz, 10-dB PAPR signal generated with the multisignal algorithm [28]. The filter anticipates the peak envelope of the sequence at $t_{\text{PK}} = 467$ ns and maintains a level which is always greater than the minimum required (Fig. 15, "no filter" case). The different minimum pulse cases demonstrate a tradeoff between PA and SM efficiency and linearity. While the finite rise and fall times and nonideal transient characteristics of the SM require a filter, a long minimum pulse time lowers PA efficiency. The effect of the filter is shown in Fig. 11, where the actual supply voltages (gray) are bounded by the ideal discretized shaping function (black). Clipping is avoided,

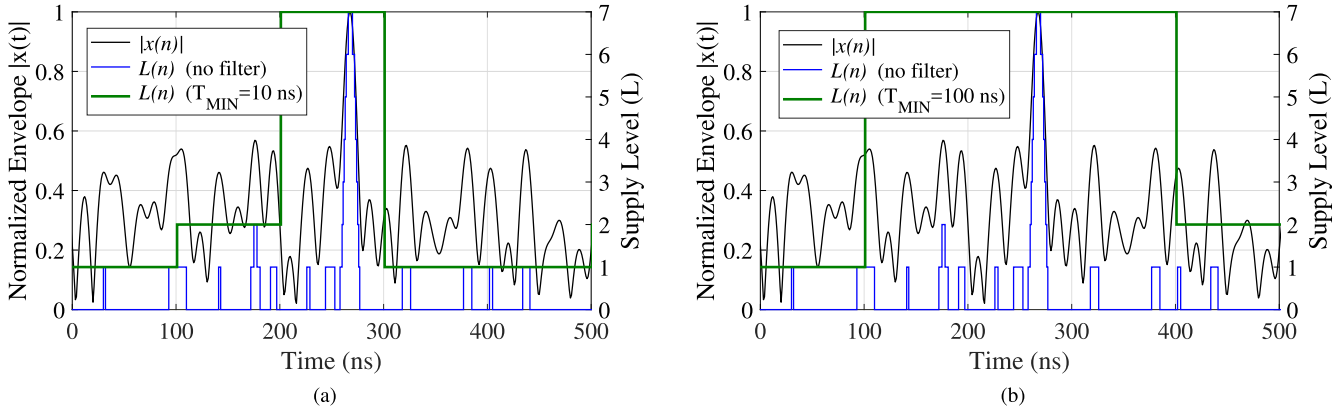

Fig. 15. Time-domain envelope of the input signal $|x(n)|$ and supply control with two different minimum pulse durations. (a) $T_{\mathrm{MIN}} = 10$ ns. (b) $T_{\mathrm{MIN}} = 100$ ns. When the filter is disabled ($T_{\mathrm{MIN}} = 0$ ns), the supply command follows the discretized shaping table with all the levels, and when the filter is used ($T_{\mathrm{MIN}} = 10$ or 100 ns), the control command loosely follows the envelope of the signal and some levels are lost.

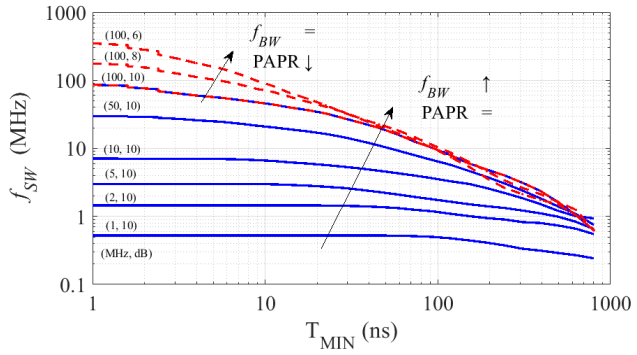

Fig. 16. Average switching frequencies f_{SW} for an eight-level quantization as a function of the minimum pulse duration T_{MIN} parameter of the max filter. The switching frequency increases with the signal bandwidth f_{BW} (blue continuous) and with lower PAPRs (red dashed). In both cases, the CRR filter presents a low-pass behavior able to reduce the average switching rate of the supply modulator, limiting power losses.

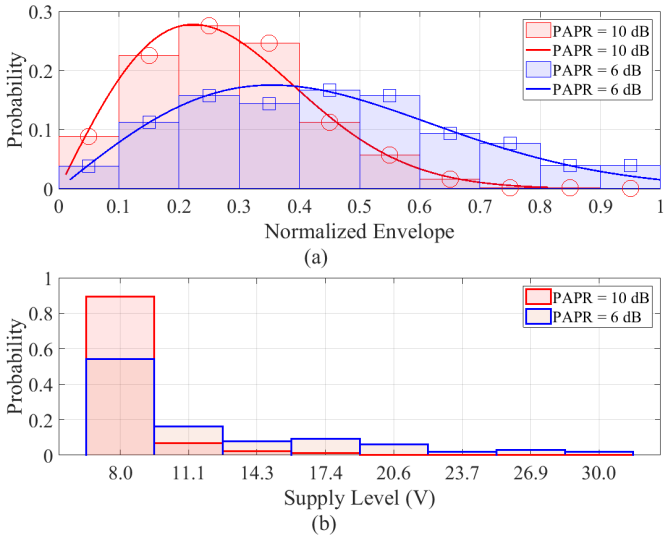

Fig. 17. (a) Histogram of two 100-MHz OFDM sequences with 6- and 10-dB PAPR. Superposed to the histogram is the most likely Rayleigh pdf. (b) Histogram showing the probability of the supply level at the output of the discretized shaping function for the two sequences. With a lower PAPR, the levels are distributed toward higher values.

but the supply level is not always optimal for efficiency. This tradeoff is explored experimentally in Section IV.

C. Filter Analysis

The filter operation is a critical part of the SM technique but cannot be analyzed using deterministic approaches due to the highly nonlinear behavior of the quantizer. The quantization error can be modeled as an additive noise source with white Gaussian distribution (if the number of levels of the quantizer is high enough) [38]. Therefore, in this section, we analyze the filter effects using a statistical approach.

Fig. 16 compiles simulations of the average switching rate of the supply modulator f_{SW}[1] for an eight-level quantization when the baseband signal bandwidth f_{BW} and PAPR are swept. Switching losses in the supply modulator are proportional to f_{SW} [39], and thus this value should be minimized. As expected, when PAPR is fixed at 10 dB and the baseband signal frequency f_{BW} is increased, f_{SW} increases (Fig. 16, blue curves).

[1] f_{SW} is the average switching rate and is defined as the number of commutations ($L(n) \neq L(n-1)$) divided by the $L(n)$ sequence length.

For a fixed signal bandwidth $f_{\mathrm{BW}} = 100$ MHz and swept PAPR, the commutation rate increases at lower PAPRs (Fig. 16, red curves). This result, although perhaps counterintuitive, is related to the quantization process. Fig. 17 compares two OFDM signals with 6- and 10-dB PAPR. As can be seen in Fig. 17(a), the 6-dB PAPR signal pdf intersects the higher envelope values with greater probability. The probability of using each supply level value is shown in Fig. 17(b); with lower PAPR, the levels are more evenly distributed, resulting in a greater number of supply modulator transitions.

When both the signal bandwidth and PAPR are fixed, the system can alternatively be analyzed in terms of the effect of T_{MIN} on the probability with which a given supply level will be used. When the filter's max algorithm is disabled ($T_{\mathrm{MIN}} = 0$), the probability of using each supply level matches that of the discretized signal as in Fig. 17. As illustrated in Fig. 18 for a 10-dB PAPR signal, increasing T_{MIN}

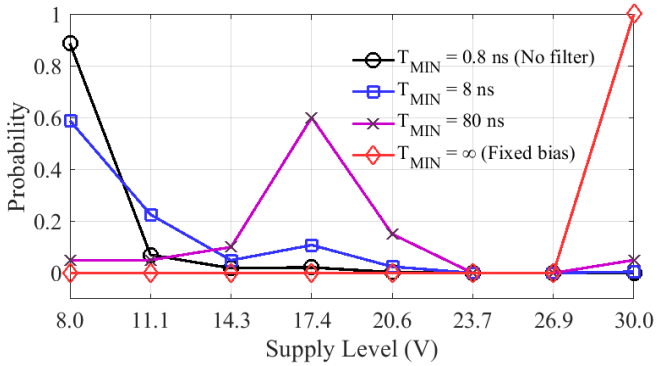

Fig. 18. Probability of each of the supply levels for a 100-MHz, 10-dB PAPR OFDM signal. When the CRR filter is disabled, the supply modulator commutates at the maximum rate ($T_{\text{MIN}} = 0.8$ ns). If the CRR filter is enabled, it is possible to increase the pulse duration (i.e., $T_{\text{MIN}} = 8$ or 80 ns), thus reducing the impact of the supply modulator switching speed. The last case corresponds to fixed bias operation ($T_{\text{MIN}} = \infty$).

redistributes the probability of using each level. The probability shifts with increasing T_{MIN} toward the limit case of $T_{\text{MIN}} = \infty$, which corresponds to the fixed bias condition. This analysis can be used to determine the required number of dc levels in a particular system and for a given T_{MIN} and signal PAPR. In this paper, the flexible efficient eight-level dynamic supply allows us to fully characterize the SM-LMBA performance across frequency and PAPR, although in practice, a reduced number of levels could be used.

D. Digital Predistortion

The I/Q test sequence is generated with the multisignal algorithm presented in [28] and with the characteristics detailed in Section III-A. The numerology $\mu = 0$ is selected which leads to a subcarrier spacing of $\Delta f = 15$ kHz. The SM-LMBA is demonstrated with an instantaneous bandwidth of $f_{\text{BW}} = 100$ MHz, which leads to 6667 carriers. The sampling frequency of the VST PXIe-5840 is selected to be 600 MHz which is enough to accommodate the targeted bandwidth of $f_{\text{BW}} = 100$ MHz and the necessary bandwidth expansion due to predistortion. The resulting I/Q sequence has $4 \cdot 10^5$ samples which are used to train and verify the DPD. The amplitudes of subcarriers are randomized while the phases are controlled to set a PAPR of 10 dB [28].

First, the architecture is tested with ideal indirect learning control (ILC) DPD to verify the feasibility of broadband signal operation and provide a performance benchmark. A gain-based learning approach is employed [40] and only two iterations are performed to optimize the modulated input sequence. Once the SM-LMBA performance is verified, a more conventional and realistic generalized memory polynomial (GMP) DPD is used with a nonlinearity order of $K_L = \{5, 5, 7, 7, 7, 7, 7, 9\}$ and a memory order of $Q_L = \{1, 3, 3, 1, 1, 1, 1, 1\}$ for the Lth level. When more levels are used, the DPD complexity increases; if $T_{\text{min}} \rightarrow \infty$ (fixed bias operation), only the last DPD model is used. In the following work, a different DPD model is extracted for each operating frequency of the SM-LMBA.

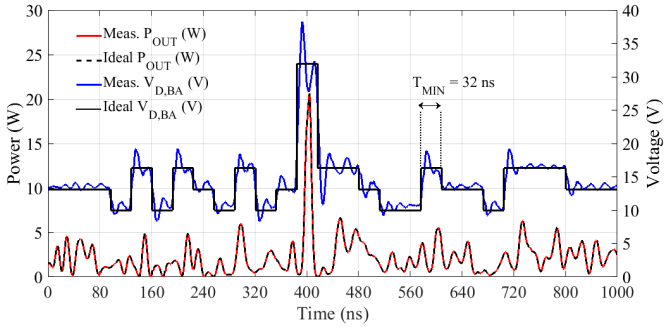

Fig. 19. Time-domain waveforms at 2.2 GHz of a 100-MHz, 10-dB PAPR signal with DPD. A minimum time step of $T_{\text{MIN}} = 32$ ns is set for the supply modulator. The ideal signal is compared to the SM-LMBA output signal with ILC DPD.

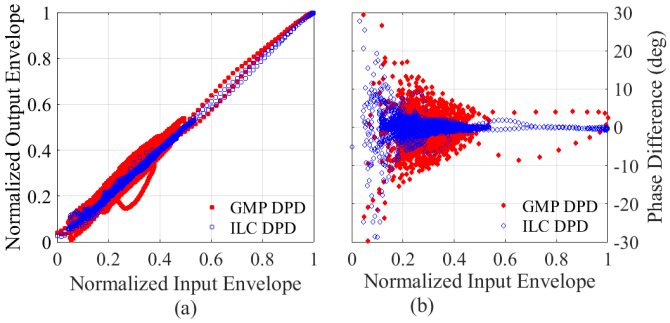

Fig. 20. (a) AM/AM and (b) AM/PM plots of the SM-LMBA driven by a 100-MHz, 10-dB PAPR signal. A minimum time step of $T_{\text{MIN}} = 32$ ns is set for the supply modulator.

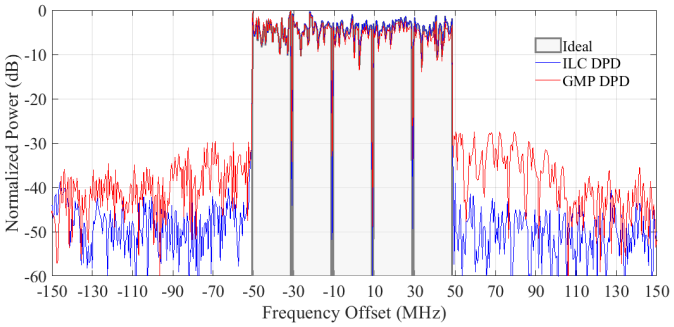

Fig. 21. Spectrum of the SM-LMBA output at 2.2 GHz of a 100-MHz, 10-dB PAPR signal with DPD. A minimum time step of $T_{\text{MIN}} = 32$ ns is set for the supply modulator. The ideal output is compared to the SM-LMBA output signal with ILC DPD and GMP DPD.

IV. SM-LMBA Measurement Results With Modulated Signals

The measurement setup in Fig. 6 is used to characterize the SM-LMBA with modulated signals. Dynamic SM is implemented using a hybrid eight-level power-DAC implemented using discrete GaN-on-Si power switches [36]. Based on a 3-bit input command, the power-DAC produces an output voltage that is the summation of three binary-scaled isolated voltage sources supplied to it. The high figure of merit of the power switches [41] results in previously demonstrated efficiencies of 92% and 83% for 1.4- and 10-MHz LTE signals,

TABLE I

PERFORMANCE COMPARISON WITH STATE-OF-THE-ART GaN WIDEBAND PAs WITH SIMILAR FREQUENCY AND OUTPUT POWER RANGE

Ref./Year	Architecture	RF inputs	Freq. (GHz)	BW (%)	Modulation BW (MHz)	P_{max} (dBm)	η @ P_{max} (%)	η @ 10 dB OBO (%)	ACLR (dBc)
[44] 2010	Broadband match	1	1.9–4.3	77	20 (LTE @ 2.5 GHz)	42	57–72	16–22*	-44
[45] 2013	Doherty-Outphasing continuum	2	1–3	100	5 (W-CDMA @ 2.3 GHz)	44.9	45–68	30–42*	-57
[46] 2014	Doherty	1	1.05–2.55	83	5 (3GPP @ 1.8 GHz)	41	45–83	28–37*	-43
[47] 2017	Doherty	1	0.55–1.1	67	20 (LTE @ 0.85 GHz)	42	60–70	24–28*	-50
[14] 2017	Octaveband LMBA	1	1.8–3.8	71	5 (W-CDMA @ 2.7 GHz)	44	46–70	22–25*	-27 †
[48] 2017	SM	1	0.7–2.1	100	80 (LTE @ 1.5 GHz)	30	-	32.1-35.5	-45
[21] 2017	SM	1	1.8	7	120 (LTE-like @ 1.8 GHz)	49	-	50.2*	-46.5
[49] 2018	SM-Doherty	1	3.5	9	60 (LTE-like @ 3.5 GHz)	42	-	58	-47
This work	SM-LMBA	1	1.8–3.8	71	100 (LTE-like @ 1.8–3.8 GHz)	44	46–70	33–64	-52

* - information derived from data in the paper, † - No DPD

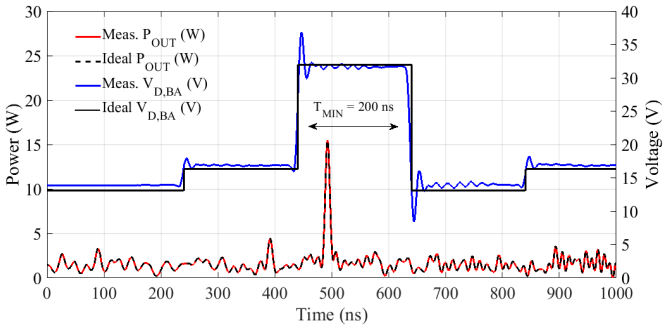

Fig. 22. Time-domain waveforms at 2.2 GHz for a 100-MHz, 10-dB PAPR signal with DPD. A minimum time step of $T_{\text{MIN}} = 200$ ns is set for the supply modulator. The ideal signal is compared to the SM-LMBA output signal with ILC DPD.

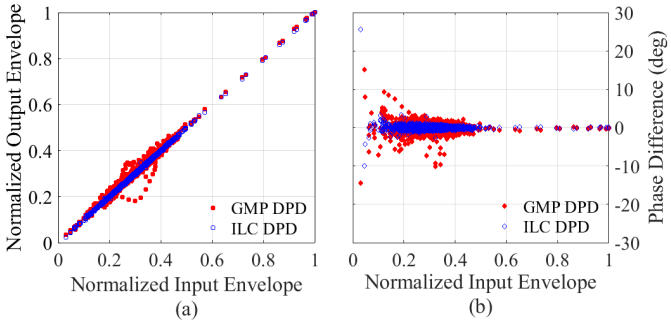

Fig. 23. (a) AM/AM and (b) AM/PM plots of the SM-LMBA driven by a 100-MHz, 10-dB PAPR OFDM signal. A minimum time step of $T_{\text{MIN}} = 200$ ns is set for the supply modulator.

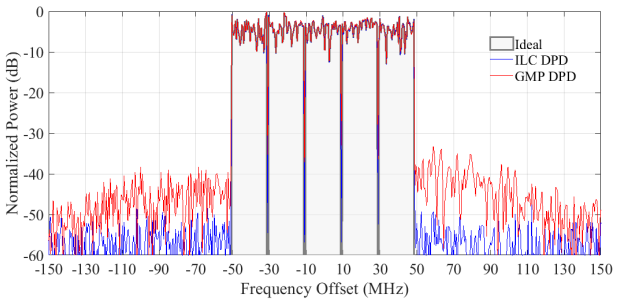

Fig. 24. Spectrum of the SM-LMBA output at 2.2 GHz of a 100-MHz, 10-dB PAPR signal with DPD. A minimum time step of $T_{\text{MIN}} = 200$ ns is set for the supply modulator. The ideal output is compared to the SM-LMBA output signal with ILC DPD and GMP DPD.

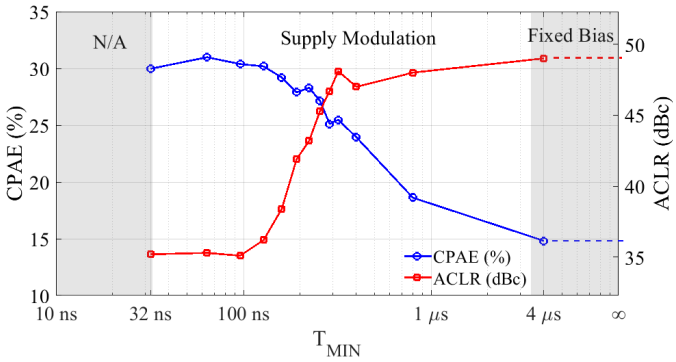

Fig. 25. Efficiency (CPAE) and linearity (ACLR) tradeoff at various minimum pulse durations (T_{MIN}) for the presented SM-LMBA driven by a 100-MHz, 10-dB PAPR signal at 2.2 GHz. At shorter T_{MIN}'s, efficiency is higher, thanks to SM, and it degrades for longer T_{MIN}'s. Conversely, ACLR linearity improves going toward fixed-bias operations. A tradeoff between efficiency and linearity is observed between 100 ns and 1 μs.

respectively [36]. This power-DAC architecture has been used to demonstrate multilevel SM of several PAs [42], including an MMIC Chireix PA [26], where the multilevel supply modulator is integrated in a GaN-on-SiC MMIC [43].

The experimental goals of this work are to validate the performance benefits of using load modulation for wideband operation combined with SM for high efficiency of high-PAPR signals. Additionally, the measurements verify the digital baseband and filtering approach described in Section III and demonstrate the effectiveness of the DPD.

Figs. 19–24 compare the time-domain waveforms, AM/AM, and AM/PM nonlinearities of the SM-LMBA at 2.2 GHz for a 100-MHz, 10-dB PAPR signal when the filter minimum time step is varied. In Figs. 19–21, the digital filter sets the minimum pulse duration of the supply modulator to be $T_{\text{MIN}} =$ 32 ns. The linearized time-domain waveforms in Fig. 19 show ringing in the BA supply voltage. This ringing is primarily a result of the resonant circuit formed by the wire interconnect between the power-DAC and PA, and the output capacitance of transistors and bias network used in the BA. In practice, this ringing will degrade the system linearity since it is not corrected for in the predistortion. It can only be reduced by careful design of the supply modulator–PA interface.

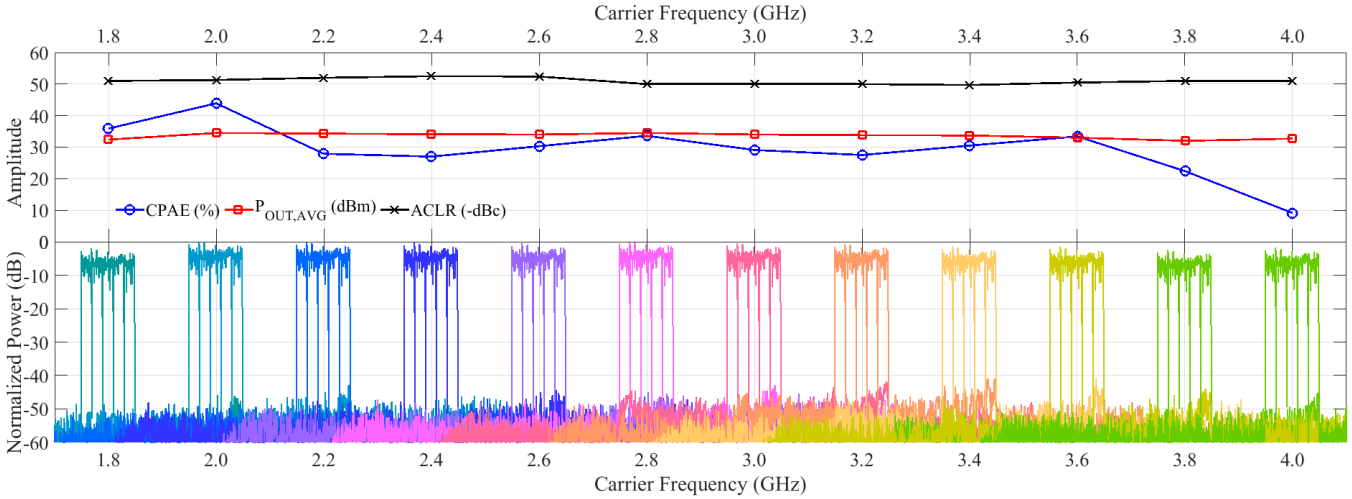

Fig. 26. Broadband performance of the SM-LMBA at different frequencies (1.8–4 GHz) with the same modulated signal with 100-MHz bandwidth and 10-dB PAPR (transmitted nonconcurrently). Iterative predistortion is used and a minimum pulse duration of $T_{\mathrm{MIN}} = 200$ ns is selected as a compromise between efficiency (CPAE) and linearity (ACLR). The linearized gain over the whole bandwidth is fixed at 9.5 dB. The spectral amplitudes are normalized to the average power $P_{\mathrm{OUT,AVG}} = 34.2$ dBm at 2.2 GHz.

The effects of the highly volatile supply voltage are apparent in Fig. 20, where the GMP described in Section III-D is unable to linearize the system. The output spectrum shows a −47-dBc ACLR with the ILC DPD and −35-dBc ACLR with the GMP.

When the minimum pulse duration is increased to 200 ns as in Figs. 22–24, the increased settling time between supply transitions results in improved linearity. This signal, with the same 100-MHz bandwidth and 10-dB PAPR as in the $T_{\mathrm{MIN}} = 32$ ns case, has a −52-dBc ACLR with the ILC DPD and −42-dBc ACLR with the GMP, but with degraded efficiency.

A study of the effects of T_{MIN} on both ACLR and efficiency is shown in Fig. 25, for a 100-MHz, 10-dB PAPR signal centered at 2.2 GHz. Here, the composite PAE (CPAE) describes the overall efficiency of the SM-LMBA, including supply modulator efficiency η_{SM}, and is defined as

$$\mathrm{CPAE} = \eta_{\mathrm{SM}}(T_{\mathrm{MIN}}) \cdot \mathrm{PAE}(T_{\mathrm{MIN}}). \tag{5}$$

As the minimum pulse time increases from 32 ns to 4 μs, the efficiency initially increases slightly due to the reduction in commutation losses within the supply modulator, but ultimately decreases as a result of the PA efficiency dependence on supply voltage (see Fig. 10). The decoupling benefit of this filter is highlighted by the ACLR improvement with increasing T_{MIN}, as expected from the results in Figs. 19–24. On the other hand, we observe that as the operation moves toward more of an averaged supply, i.e., $T_{\mathrm{MIN}} \to \infty$, the supply modulator losses are mostly ascribable to the conduction losses in the power switches of the supply modulator and the static driving losses in the driving circuitry [36]. Here, an ACLR of −49 dBc and CPAE of 14.8% are observed which are also representative of the LMBA operated with fixed bias. For this system, we select $T_{\mathrm{MIN}} = 200$ ns as a compromise between linearity and composite efficiency.

The SM-LMBA is evaluated over 1.8–4 GHz with a 100-MHz, 10-dB PAPR signal as summarized in Fig. 26. At each center frequency, characterized nonconcurrently, the same modulated signal is used. A minimum pulse duration of $T_{\mathrm{MIN}} = 200$ ns is used in each case, along with ILC predistortion. In order to directly compare the composite PAE and average output power at each center frequency, the linearized gain is fixed at 9.5 dB over the entire bandwidth. The SM-LMBA shows consistent performance across an octave band, with composite PAE ranging from 43.9% to 22.4% across 1.8–3.8 GHz, and with ACLR values approximately constant at −52 dBc. Compared to the pulsed CW measurements of the SM-LMBA in Fig. 9, the shape of the efficiency across the band is as expected.

A summary of state-of-the-art GaN PAs with similar frequency and output power range is given in Table I. In comparison, this paper shows a substantially higher modulation bandwidth over a large RF frequency range. In [21], a 120-MHz signal is amplified using SM, demonstrating very high efficiency at 10-dB output back off, but the PA itself is narrowband around 1.8 GHz. Furthermore, the performance advantage of the SM-LMBA compared to the LMBA without SM can be seen in the higher efficiency at 10-dB output back off. Overall, the SM-LMBA compares favorably to the state of the art and is well-suited for 5G-like signals.

V. Conclusion

This paper presents the application of the discrete-level SM to an RF-input LMBA for broadband, efficient amplification. The PA design targets 5G sub-6-GHz systems, where wideband high-PAPR OFDM signals place demanding requirements on PA performance. In the SM-LMBA technique, the broadband operation is achieved through active matching within the RF-input LMBA PA, while back-off efficiency is extended through SM. Based on our study of SM approaches for the LMBA, a modulated BA supply with fixed control amplifier supply is found to be the most practical solution while still giving performance benefits. This paper extends the related conference paper, presenting a detailed investigation

of how digital filtering within the discrete-level SM tradeoffs efficiency and linearity, and validating the theory through PA characterization using 100-MHz signals. The digital filtering approach, in which a minimum duration T_{MIN} is enforced between each supply level transition, decouples the performance of the supply-modulated PA from the signal characteristics (i.e., PAPR) and bandwidth.

The SM-LMBA is demonstrated with fixed control amplifier supply voltage and modulated BA supply voltage for a generalized OFDM-like signal with 100-MHz bandwidth and 10-dB PAPR across its 1.8–4-GHz operating range. The characterization of CPAE and ACLR versus the minimum pulse duration T_{MIN} clearly shows an efficiency-linearity tradeoff at a given frequency point. For this system, a 200-ns T_{MIN} value represents a good compromise between linearity and CPAE. When this value is applied and ILC predistortion is used for linearization, the SM-LMBA shows consistently good performance across the band, with ACLR values approximately constant at -52 dBc, and 22.4%–43.9% average CPAE matching the expected characteristics from the pulsed characterization.

ACKNOWLEDGMENT

Authors T. Cappello and T. W. Barton would like to thank Tektronix for the loan by Tektronix of the 5 Series mixed signal oscilloscope used for the time-domain supply voltage and current measurements. Author Z. Popovic would like to thank the Lockheed Martin Endowed Chair of RF Engineering and a gift and equipment support from National Instruments.

REFERENCES

[1] A. A. Zaidi *et al.*, "Waveform and numerology to support 5G services and requirements," *IEEE Commun. Mag.*, vol. 54, no. 11, pp. 90–98, Nov. 2016.

[2] S. H. Han and J. H. Lee, "An overview of peak-to-average power ratio reduction techniques for multicarrier transmission," *IEEE Wireless Commun.*, vol. 12, no. 2, pp. 56–65, Apr. 2005.

[3] B. Kim, J. Kim, I. Kim, and J. Cha, "The Doherty power amplifier," *IEEE Microw. Mag.*, vol. 7, no. 5, pp. 42–50, Oct. 2006.

[4] W. H. Doherty, "A new high efficiency power amplifier for modulated waves," *Proc. IRE*, vol. 24, no. 9, pp. 1163–1182, Sep. 1936.

[5] W. Hallberg, M. Özen, D. Gustafsson, K. Buisman, and C. Fager, "A Doherty power amplifier design method for improved efficiency and linearity," *IEEE Trans. Microw. Theory Techn.*, vol. 64, no. 12, pp. 4491–4504, Dec. 2016.

[6] L. Piazzon *et al.*, "Effect of load modulation on phase distortion in Doherty power amplifiers," *IEEE Microw. Wireless Compon. Lett.*, vol. 24, no. 7, pp. 505–507, Jul. 2014.

[7] H. Chireix, "High power outphasing modulation," *Proc. Inst. Radio Eng.*, vol. 23, no. 11, pp. 1370–1392, Nov. 1935.

[8] T. W. Barton, A. S. Jurkov, P. H. Pednekar, and D. J. Perreault, "Multi-way lossless outphasing system based on an all-transmission-line combiner," *IEEE Trans. Microw. Theory Techn.*, vol. 64, no. 4, pp. 1313–1326, Apr. 2016.

[9] D. A. Calvillo-Cortes *et al.*, "A package-integrated Chireix outphasing RF switch-mode high-power amplifier," *IEEE Trans. Microw. Theory Techn.*, vol. 61, no. 10, pp. 3721–3732, Oct. 2013.

[10] A. Huttunen and R. Kaunisto, "A 20-W Chireix outphasing transmitter for WCDMA base stations," *IEEE Trans. Microw. Theory Techn.*, vol. 55, no. 12, pp. 2709–2718, Dec. 2007.

[11] D. J. Shepphard, J. Powell, and S. C. Cripps, "An efficient broadband reconfigurable power amplifier using active load modulation," *IEEE Microw. Wireless Compon. Lett.*, vol. 26, no. 6, pp. 443–445, Jun. 2016.

[12] R. Quaglia and S. Cripps, "A load modulated balanced amplifier for telecom applications," *IEEE Trans. Microw. Theory Techn.*, vol. 66, no. 3, pp. 1328–1338, Mar. 2018.

[13] J. R. Powell, D. J. Shepphard, R. Quaglia, and S. C. Cripps, "A power reconfigurable high-efficiency X-band power amplifier MMIC using the load modulated balanced amplifier technique," *IEEE Microw. Wireless Compon. Lett.*, vol. 28, no. 6, pp. 527–529, Jun. 2018.

[14] P. H. Pednekar, E. Berry, and T. W. Barton, "RF-input load modulated balanced amplifier with octave bandwidth," *IEEE Trans. Microw. Theory Techn.*, vol. 65, no. 12, pp. 5181–5191, Dec. 2017.

[15] P. Asbeck and Z. Popovic, "ET comes of age: Envelope tracking for higher-efficiency power amplifiers," *IEEE Microw. Mag.*, vol. 17, no. 3, pp. 16–25, Mar. 2016.

[16] J. Jeong *et al.*, "High-efficiency WCDMA envelope tracking base-station amplifier implemented with GaAs HVHBTs," *IEEE J. Solid-State Circuits*, vol. 44, no. 10, pp. 2629–2639, Oct. 2009.

[17] V. Yousefzadeh, E. Alarcon, and D. Maksimovic, "Efficiency optimization in linear-assisted switching power converters for envelope tracking in RF power amplifiers," in *Proc. IEEE Int. Symp. Circuits Syst.*, vol. 2, May 2005, pp. 1302–1305.

[18] J. Choi *et al.*, "A 45/46/34% PAE linear polar transmitter for EDGE/WCDMA/Mobile-WiMax," in *IEEE MTT-S Int. Microw. Symp. Dig.*, Jun. 2009, pp. 413–416.

[19] J. Jeong, D. F. Kimball, M. Kwak, C. Hsia, P. Draxler, and P. M. Asbeck, "Wideband envelope tracking power amplifiers with reduced bandwidth power supply waveforms and adaptive digital predistortion techniques," *IEEE Trans. Microw. Theory Techn.*, vol. 57, no. 12, pp. 3307–3314, Dec. 2009.

[20] M. Olavsbråten and D. Gecan, "Bandwidth reduction for supply modulated RF PAs using power envelope tracking," *IEEE Microw. Wireless Compon. Lett.*, vol. 27, no. 4, pp. 374–376, Apr. 2017.

[21] N. Wolff, W. Heinrich, and O. Bengtsson, "Highly efficient 1.8-GHz amplifier with 120-MHz class-G supply modulation," *IEEE Trans. Microw. Theory Techn.*, vol. 65, no. 12, pp. 5223–5230, Dec. 2017.

[22] P. Medrel *et al.*, "Implementation of dual gate and drain dynamic voltage biasing to mitigate load modulation effects of supply modulators in envelope tracking power amplifiers," in *IEEE MTT-S Int. Microw. Symp. Dig.*, Jun. 2014, pp. 1–4.

[23] J. Moon *et al.*, "Doherty amplifier with envelope tracking for high efficiency," in *IEEE MTT-S Int. Microw. Symp. Dig.*, May 2010, pp. 1086–1089.

[24] A. Alt and J. Lees, "Improving efficiency, linearity and linearisability of an asymmetric Doherty power amplifier by modulating the peaking Amplifier's supply voltage," in *Proc. Eur. Microw. Conf.*, Oct. 2017, pp. 464–467.

[25] D. Fishler *et al.*, "A study of supply modulation applied to a Doherty power amplifier," in *Proc. IEEE Eur. Microw. Conf.*, 2018, pp. 1–4.

[26] T. Cappello, T. W. Barton, C. Florian, M. Litchfield, and Z. Popovic, "Multilevel supply-modulated chireix outphasing with continuous input modulation," *IEEE Trans. Microw. Theory Techn.*, vol. 65, no. 12, pp. 5231–5243, Dec. 2017.

[27] T. Cappello, P. H. Pednekar, C. Florian, Z. Popovic, and T. W. Barton, "Supply modulation of a broadband load modulated balanced amplifier," in *IEEE/MTT-S Int. Microw. Symp. Dig.*, Jun. 2018, pp. 1–4.

[28] T. Cappello, A. Duh, T. W. Barton, and Z. Popovic, "A dual-band dual-output power amplifier for carrier aggregation," *IEEE Trans. Microw. Theory Techn.*, to be published.

[29] S. H. Müller, R. W. Bäuml, R. F. Fischer, and J. B. Huber, "OFDM with reduced peak-to-average power ratio by multiple signal representation," *Ann. Telecommun.*, vol. 52, nos. 1–2, pp. 58–67, Jan. 1997.

[30] M. Shafi *et al.*, "5G: A tutorial overview of standards, trials, challenges, deployment, and practice," *IEEE J. Sel. Areas Commun.*, vol. 35, no. 6, pp. 1201–1221, Jun. 2017.

[31] *5G New Radio Modulation Analysis Option BHN 89600 VSA Software*, Keysight Technol., Santa Rosa, CA, USA, Feb. 2018.

[32] M. Lichtman *et al.*, "5G NR jamming, spoofing, and sniffing: Threat assessment and mitigation," in *Proc. IEEE Int. Conf. Commun. Workshops*, May 2018, pp. 1–6.

[33] X. Li and L. J. Cimini, "Effects of clipping and filtering on the performance of OFDM," *IEEE Commun. Lett.*, vol. 2, no. 5, pp. 131–133, May 1998.

[34] P. P. Ann and R. Jose, "Comparison of PAPR reduction techniques in OFDM systems," in *Proc. Int. Conf. Commun. Electr. Syst.*, Oct. 2016, pp. 1–5.

[35] H. Cao, C. Fager, T. Khan, A. S. Tehrani, and T. Eriksson, "Comparison of bandwidth reduction schemes in dynamic load modulation power amplifier architectures," in *Proc. Workshop Integr. Nonlinear Microw. Millim.-Wave Circuits (INMMIC)*, Apr. 2011, pp. 1–4.

[36] C. Florian, T. Cappello, R. P. Paganelli, D. Niessen, and F. Filicori, "Envelope tracking of an RF high power amplifier with an 8-level digitally controlled GaN-on-Si supply modulator," *IEEE Trans. Microw. Theory Techn.*, vol. 63, no. 8, pp. 2589–2602, Aug. 2015.
[37] A. Cesari, A. Cid-Pastor, C. Alonso, and J.-M. Dilhac, "A DSP structure authorizing reduced-bandwidth DC/DC converters for dynamic supply of RF power amplifiers in wideband applications," in *Proc. Conf. IEEE Ind. Electr.*, Nov. 2006, pp. 3361–3366.
[38] T. Carusone, D. Johns, and K. Martin, *Analog Integrated Circuit Design*, 2nd ed. Hoboken, NJ, USA: Wiley, 2011.
[39] N. Mohan, T. M. Undeland, and W. P. Robbins, *Power Electronics: Converters, Applications and Design*. Hoboken, NJ, USA: Wiley, 2002.
[40] J. Chani-Cahuana, P. N. Landin, C. Fager, and T. Eriksson, "Iterative learning control for RF power amplifier linearization," *IEEE Trans. Microw. Theory Techn.*, vol. 64, no. 9, pp. 2778–2789, Sep. 2016.
[41] T. Cappello, A. Santarelli, and C. Florian, "Dynamic RON characterization technique for the evaluation of thermal and off-state voltage stress of GaN switches," *IEEE Trans. Power Electron.*, vol. 33, no. 4, pp. 3386–3398, Apr. 2018.
[42] C. Florian, T. Cappello, D. Niessen, R. P. Paganelli, S. Schafer, and Z. Popović, "Efficient programmable pulse shaping for *X*-band GaN MMIC radar power amplifiers," *IEEE Trans. Microw. Theory Techn.*, vol. 65, no. 3, pp. 881–891, Mar. 2017.
[43] T. Cappello, C. Florian, D. Niessen, R. P. Paganelli, and S. Schafer, "Efficient X-band transmitter with integrated GaN power amplifier and supply modulator," *IEEE Trans. Microw. Theory Techn.*, vol. 67, no. 4, pp. 1601–1614, Apr. 2019.
[44] P. Saad, C. Fager, H. Cao, H. Zirath, and K. Andersson, "Design of a highly efficient 2–4-GHz octave bandwidth GaN-HEMT power amplifier," *IEEE Trans. Microw. Theory Techn.*, vol. 58, no. 7, pp. 1677–1685, Jul. 2010.
[45] C. M. Andersson, D. Gustafsson, J. C. Cahuana, R. Hellberg, and C. Fager, "A 1–3-GHz digitally controlled dual-RF input power-amplifier design based on a Doherty-outphasing continuum analysis," *IEEE Trans. Microw. Theory Techn.*, vol. 61, no. 10, pp. 3743–3752, Oct. 2013.
[46] R. Giofrè, L. Piazzon, P. Colantonio, and F. Giannini, "A closed-form design technique for ultra-wideband Doherty power amplifiers," *IEEE Trans. Microw. Theory Techn.*, vol. 62, no. 12, pp. 3414–3424, Dec. 2014.
[47] R. Darraji, D. Bhaskar, T. Sharma, M. Helaoui, P. Mousavi, and F. M. Ghannouchi, "Generalized theory and design methodology of wideband Doherty amplifiers applied to the realization of an octave-bandwidth prototype," *IEEE Trans. Microw. Theory Techn.*, vol. 65, no. 8, pp. 3014–3023, Aug. 2017.
[48] S. Sakata *et al.*, "An 80 MHz modulation bandwidth high efficiency multi-band envelope-tracking power amplifier using GaN single-phase buck-converter," in *IEEE MTT-S Int. Microw. Symp. Dig.*, Jun. 2017, pp. 1854–1857.
[49] D. Fishler, T. Cappello, W. Hallberg, T. Barton, and Z. Popovic, "Supply modulation of a linear Doherty power amplifier," in *Proc. Eur. Microw. Conf.*, Sep. 2018, pp. 1–5.

Tommaso Cappello (S'13–M'17) received the Laurea degree *(cum laude)* in electrical engineering and the Ph.D. degree from the University of Bologna, Bologna, Italy, in 2013 and 2017, respectively.

Since 2017, he has been a Research Associate with the Microwave and RF Research Group, University of Colorado Boulder, Boulder, CO, USA. His current research interests include the design, characterization and modeling of RF power amplifiers in efficient transmitters for radar and communications, and high-voltage GaN device characterization and modeling for power electronics.

Prathamesh Pednekar (S'15) received the B.E. degree in electronics and telecommunication engineering from the University of Mumbai, Mumbai, India, in 2012, and the M.S. degree in electrical engineering from the University of Texas at Dallas, Dallas, TX, USA, in 2016. He is currently pursuing the Ph.D. degree at the University of Colorado Boulder, Boulder, CO, USA.

From 2012 to 2014, he was a Research Scientist with the Society for Applied Microwave Electronic Engineering and Research, Mumbai. His current research interests include efficient power amplifier architectures, passive microwave components, and phased array RADARs.

Mr. Pednekar was a recipient of Best Student Paper Award of IEEE Radio Wireless Week (RWW2016).

Corrado Florian (S'02–M'04) received the Ph.D. degree in electronic and computer science engineering from the University of Bologna, Bologna, Italy, in 2004.

He is currently a Research Associate with the Department of Electrical, Electronic and Information Engineering (DEI), University of Bologna, where he is a Lecturer of high-frequency electronic circuits and devices and power electronics. His current research interests include microwave monolithic circuit design, hybrid RF circuit design, nonlinear dynamic system characterization and modeling, microwave and millimeter-wave device characterization and modeling, and power electronic circuits.

Steve Cripps (M'81–SM'90–F'11–LF'16), photograph and biography not available at the time of publication.

Zoya Popovic (S'86–M'90–SM'99–F'02) received the Dipl.Ing. degree from the University of Belgrade, Belgrade, Serbia, and the Ph.D. degree from the California Institute of Technology, Pasadena, CA, USA.

In 2001, she was a Visiting Professor with the Technical University of Munich, Munich, Germany. In 2014, she was a Visiting Professor with International Standards for Assurance Engagements (ISAE), Toulouse, France. She is currently a Distinguished Professor and the Lockheed Martin Endowed Chair of Electrical Engineering with the University of Colorado at Boulder, Boulder, CO, USA. She has graduated 58 Ph.D. students and currently advises 12 doctoral students. Her research interests include high-efficiency power amplifiers and transmitters, microwave and millimeter-wave high-performance circuits for communications and radar, medical applications of microwaves, millimeter-wave and tetrahertz quasi-optical techniques and wireless powering.

Ms. Popovic was elected as a Foreign Member of the Serbian Academy of Sciences and Arts in 2006. She was a recipient of two IEEE MTT-S Microwave Prizes for best journal papers, the White House NSF Presidential Faculty Fellow Award, the URSI Issac Koga Gold Medal, the ASEE/HP Terman Medal, and the German Humboldt Research Award. She was named the Chair of Excellence at Carlos III University of Madrid in 2018. She was the IEEE MTT-S Distinguished Educator in 2013 and the University of Colorado Distinguished Research Lecturer in 2015.

Taylor W. Barton (S'07–M'12–SM'19) received the Sc.B., M.Eng., E.E., and Sc.D. degrees from the Massachusetts Institute of Technology, Cambridge, MA, USA.

She was a Post-Doctoral Associate with the MIT Microsystems Technology Laboratories. She was an Assistant Professor with The University of Texas at Dallas, Dallas, TX, USA. In 2016, she joined the Department of Electrical, Computer, and Energy Engineering, University of Colorado at Boulder, Boulder, CO, USA, where she is currently an Assistant Professor and holds the Lockheed Martin Faculty Fellowship for outstanding junior faculty.

Ms. Barton was a recipient of the AFOSR Young Investigator Award and the NSF CAREER Award.